CrystEngComm

PAPER

View Article Online
View Journal | View Issue

Cite this: *CrystEngComm*, 2014, **16**, 10227

Co_3O_4 nanostructures with a high rate performance as anode materials for lithium-ion batteries, prepared *via* book-like cobalt–organic frameworks†

Bo Yan,[ab] Lin Chen,[ab] Yuanjun Liu,[a] Guoxing Zhu,[a] Chunguang Wang,[b] Han Zhang,[b] Gang Yang,*[b] Haitao Ye[c] and Aihua Yuan*[a]

Received 24th June 2014,
Accepted 15th September 2014

DOI: 10.1039/c4ce01277a

www.rsc.org/crystengcomm

The self-assembly of cobalt coordination frameworks (Co-CPs) with a two-dimensional morphology is demonstrated by a solvothermal method. The morphology of the Co-CPs has been controlled by various solvothermal conditions. The two-dimensional nanostructures agglomerated by Co_3O_4 nanoparticles remained after the pyrolysis of the Co-CPs. The as-synthesized Co_3O_4 anode material is characterized by cyclic voltammetry (CV), electrochemical impedance spectroscopy (EIS) and galvanostatic charge–discharge measurements. The morphology of Co_3O_4 plays a crucial role in the high performance anode materials for lithium batteries. The Co_3O_4 nanoparticles with opened-book morphology deliver a high capacity of 597 mA h g^{-1} after 50 cycles at a current rate of 800 mA g^{-1}. The opened-book morphology of Co_3O_4 provides efficient lithium ion diffusion tunnels and increases the electrolyte/Co_3O_4 contact/interfacial area. At a relatively high current rate of 1200 mA g^{-1}, Co_3O_4 with opened-book morphology delivers an excellent rate capability of 574 mA h g^{-1}.

1 Introduction

Rechargeable lithium-ion batteries (LIBs) are considered to be some of the most important energy storage systems for the ever-growing demand for portable products and electric vehicles owing to their lightweight nature, high energy density, and durable cycling life. Commercial graphite anodes for lithium batteries offer both electrochemical and mechanical stability, but provide a low theoretical capacity of 372 mA h g^{-1} and poor rate performance.[1] Alloy anode materials with higher capacities, low cost and environmentally benign elements such as silicon and tin, have attracted more interest as replacements for carbon-based anodes.[2] However, large volume changes and metal aggregation take place during the lithium alloying and de-alloying processes, and significant capacity fading during cycling has therefore hindered the further development of metallic material.[3]

To clear the above hurdle, transition metal oxides, such as Co_3O_4, SnO_2, FeO_x, MnO_x and NiO, *etc*,[4–7] have been widely studied as potential anode materials for LIBs due to their high specific capacities, high rate performance and stability. Co_3O_4 is an ideal anode material for LIBs. Wang *et al.*[8] synthesized Co_3O_4 nanotubes, which have shown an excellent rate capability and a high capacity after a number of cycles. The properties of the as-synthesized Co_3O_4 nanocrystals strongly depend on their morphology and grain size. Therefore, developing shape-controlled Co_3O_4 with a high performance as anode materials for LIBs has attracted great research interest in recent years. Many efforts have been made to design and develop effective methods to synthesize Co_3O_4 with different morphologies, including one-dimensional (1D) nanorods, two-dimensional (2D) nanosheets and three-dimensional (3D) nanostructures.[9–15]

However, Co_3O_4 is cubic and lacks structural anisotropy for 1D or 2D growth.[16] A promising approach to synthesizing Co_3O_4 with a designed structure and morphology is a morphology-conserved transformation from its precursors. For example, Zhan and co-workers[17] prepared porous Co_3O_4 nanosheets based on controlled thermal oxidative decomposition and recrystallization of precursor $Co(OH)_2$ hexagonal nanosheets. Wang *et al.*[18] synthesized Co_3O_4 from the precursors obtained from the reaction of cobalt acetate with ethylene glycol (EG) in the presence of the surfactant

[a] *School of Biology and Chemical Engineering, Jiangsu University of Science and Technology, Zhenjiang 212003, PR China. E-mail: aihuayuan@163.com*
[b] *School of Chemistry & Materials Engineering, Changshu Institute of Technology, Changsu, 215500, PR China. E-mail: gyang@cslg.edu.cn*
[c] *School of Engineering and Applied Science, Aston University, Birmingham B4 7ET, UK*

† Electronic supplementary information (ESI) available. See DOI: 10.1039/c4ce01277a

polyvinylpyrrolidone (PVP). Li *et al.*[19] synthesized Co_3O_4 from β-$Co(OH)_2$ nanosheets and $Co(CO_3)_{0.5}(OH)_{0.11}H_2O$ nanobelts as precursors *via* a solvothermal route. Recently, coordination polymers (CPs) with metal organic frameworks have been proven to be useful precursors for fabricating the corresponding morphology preserved metal oxide.[20–24] Until now, few studies have been done on the facile and controllable synthesis of Co_3O_4 nanostructures derived from the pyrolysis of Co-based CPs or metal organic frameworks (MOFs).[25,26]

In this work, we focus on the self-assembly of Co coordination polymers (Co-CPs) with a two-dimensional morphology by a solvothermal method, in which the two-dimensional agglomerated nanoparticles of Co_3O_4 remained after pyrolysis. The crystal structures and morphologies of the Co-CPs and Co_3O_4 are characterized by X-ray diffraction patterns (XRD), FTIR, TGA, SEM and TEM. The as-prepared Co_3O_4 with various 2D morphologies are evaluated for their potential use as anode materials for LIBs in detail.

2 Experimental

2.1 Material syntheses

Synthesis of the Co-CPs. In a typical preparation procedure, 0.5 mmol of $Co(NO_3)_2{\cdot}6H_2O$, 0.5 of mmol 1,3,5-benzenetricarboxylic acid (BTC) and 3 mmol of pyrazine were dissolved in 30 mL of *N*,*N*-dimethylformamide (DMF) under vigorous stirring for 30 min. The mixture was transferred into a Teflon autoclave with 50 mL capacity, and maintained at 100 °C for 10, 12 and 24 h, respectively. The obtained precipitates were collected by centrifugation, washed with ethanol several times and dried at 60 °C in a vacuum. The produced samples are simply named Co-CP-A, Co-CP-B and Co-CP-C, according to the solvothermal time of 10, 12 and 24 h, respectively.

Synthesis of the Co_3O_4 nanomaterials. The Co-CP materials were pyrolyzed in a tube furnace at 500 °C for 30 min in air. The heating rate was controlled at 1 °C min^{-1}. The as-synthesized metal oxides are simply named Co_3O_4-A, Co_3O_4-B and Co_3O_4-C, respectively.

2.2 Characterization

X-ray diffraction studies were performed using a Rigaku diffractometer (DMax-2200) with Cu Kα radiation. The diffraction data were collected at a scan rate of 4° min^{-1} from 5 to 80°. FTIR spectra of KBr powder pressed pellets were recorded on a Bruker VECTOR 22 spectrometer. The morphology was characterized using a field emission scanning electron microscope (FESEM, Zeiss Sigma microscope, 20 kV), and a TEM (JEOL-2000CX, 200 kV). The specific surface area was obtained from the N_2 adsorption–desorption isotherms using a Micromeritics ASAP 2020 M + C nitrogen adsorption instrument (Micromeritics Inc., USA) at 77 K.

2.3 Electrochemical measurements

Electrochemical measurements were carried out using a coin cell (CR2016). The composite cathode was formulated with active materials (70 wt%), Super P (20 wt%) and poly(vinylidene fluoride) (10 wt%) mixed with *N*-methyl-2-pyrrolidone. After being stirred for 2 h, the slurry was cast onto Cu foil using a doctor blade, and dried at 120 °C for 12 h under vacuum. The coin cells were assembled in an argon-filled glove box using lithium as the negative electrodes, Celgard 2500 as the separators, and 1 M $LiPF_6$ (dissolved in ethylene carbonate, dimethyl carbonate and ethyl methyl carbonate, with a 1 : 1 : 1 volume ratio) as the electrolytes. The galvanostatic charge and discharge experiments were carried out at room temperature using a LAND CT2001A (Wuhan, China) and the cut-off voltage ranged from 0 to 3 V. Cyclic voltammetry (CV) was conducted on a PARSTAT2273 electrochemical workstation (Princeton Applied Research, USA) at a scanning rate of 0.1 mV s^{-1} in the potential range of 0–3 V. Electrochemical impedance spectroscopy (EIS) measurements were conducted on the PARSTAT2273 electrochemical workstation; the amplitude of the input ac signal was kept at 5 mV and the frequency range was set between 100 kHz and 0.1 mHz. A two-electrode cell was used for the impedance measurement, and a lithium foil acted as both the counter electrode and the reference electrode.

3 Results and discussion

3.1 Structural and morphological characterization

For a tunable morphology of Co_3O_4 after the pyrolysis of the Co-CPs, Co cation complexes with the ligands of BTC and pyrazine are first produced and the crystal morphology is controlled by various solvothermal conditions. However, the molecular structures of the as-synthesized Co-CPs cannot be presented because the corresponding single crystals suitable for X-ray measurements cannot be obtained. Instead, the single crystals can only be obtained when the concentrations of the reactants decrease, but their XRD patterns do not match with the Co-CP crystals produced at a large scale. A powder XRD pattern of the Co-CPs is presented in Fig. S1 (ESI†) which shows the high crystallinity of the Co complex, but no standard PDF cards match with the XRD pattern of the Co-CPs. The XRD patterns of Co-CP-A, Co-CP-B and Co-CP-C are the same, indicating that the same phases were obtained at different reaction times.

Fig. 1 shows the SEM images and schematic morphologies of the samples before and after pyrolysis. The solvothermal time plays a crucial role in the formation of the Co-CPs with different morphologies. At 10 h, separate nanosheets are formed with regular shapes like pieces of nanopaper (Fig. 1a). After 12 h, the nanopapers are self-assembled like an opened book (Fig. 1b). When the reaction time is extended to 24 h, the nanosheets are densely self-packed and the morphology of Co-CP-C looks like a closed book (Fig. 1c).

The strategy for synthesizing the Co_3O_4 is schematically depicted in Fig. 1d. The crystal growth of the nanomaterials is modulated extrinsically in accordance with the selective adsorption of the solvents, inorganic additives and surfactants to certain crystallographic planes. The selective

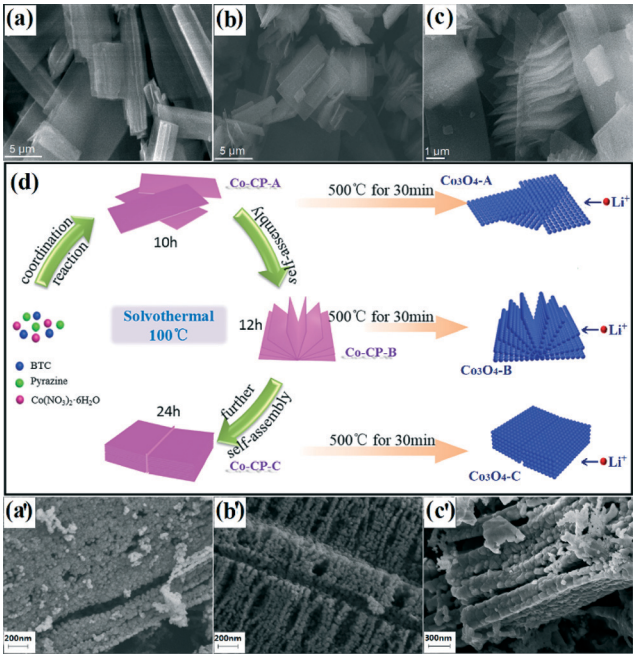

Fig. 1 SEM images of (a) Co-CP-A, (b) Co-CP-B and (c) Co-CP-C. (d) Schematic illustration showing the evolution of the Co-CPs with reaction time and the formation of the porous Co_3O_4 aggregates. SEM images of (a′) Co_3O_4-A, (b′) Co_3O_4-B and (c′) Co_3O_4-C.

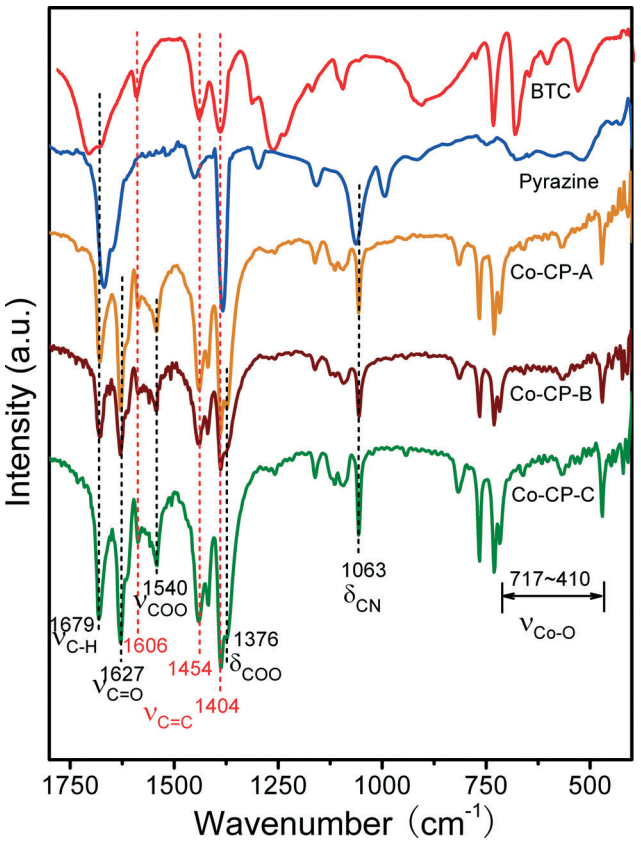

Fig. 2 FTIR spectra of the Co-CPs and the ligands of pyrazine and BTC.

adsorption based on the surface energy determines the growth of the crystal planes leading to a specific shape of the material.[27] Co-CPs with tunable morphologies are developed through a typical solvothermal method (as shown in Fig. 1d). The ligands of BTC and pyrazine are coordinated and jointly react with $Co(NO_3)_2{\cdot}6H_2O$ to form the well-organized sheet (Co-CP-A) within a short solvothermal time.

Afterwards the nanosheets are self-assembled to the opened book-like morphology (Co-CP-B), and then change to the overlapped morphology (Co-CP-C) at long solvothermal times. After subsequent pyrolysis, the Co-CPs convert to Co_3O_4. The as-synthesized Co_3O_4 almost has the same morphology as the precursor Co-CPs (as shown in Fig. 1a′–c′). Highly interconnected/aggregated nanoparticles are observed with an average size of 20–30 nm. The Co-CPs provide an efficient way to facilitate the formation of the tunable morphology of Co_3O_4.

The structures and components of the Co-CPs are elucidated by FTIR, as shown in Fig. 2. The characteristic peaks at 1606, 1454 and 1404 cm^{-1} are attributed to the stretching vibrations of the benzenoid rings of BTC. The peaks at 1063 cm^{-1} correspond to the C=N stretching mode of pyrazine.[28] It is believed that these are the coordination bonds of the Co cations with the ligands of BTC and pyrazine after solvothermal treatment. The absence of absorption bands at 1730–1690 cm^{-1} where the –COOH peak is expected to appear is indicative of the deprotonation of BTC upon reaction with the metal ions.[29] The relatively strong absorption at 1540 cm^{-1} is the characteristic ν_s(O–Co) stretching mode of the carboxylate groups with the Co cations.[25] The weak bands between 717 and 470 cm^{-1} are assigned to the asymmetric and symmetric stretching modes of the coordinated Co–O groups, respectively. As shown in Fig. 2, the Co-CPs obtained by the solvothermal method for 10, 12 and 24 h present very similar FTIR spectra, indicating that the same or similar Co complexes with various crystal morphologies are obtained.

The thermal decomposition behavior of the Co-CPs is analysed by TGA as shown in Fig. S2 (ESI†). The weight loss before 300 °C has been measured to be 40.5%, which is attributed to the removal of the volatile solvent DMF, water molecules and some other small molecules. The second predominant weight loss (~33.7%) occurs at ~450 °C and is ascribed to the decomposition and subsequent oxidation of the benzene tricarboxylic group. There is a small weight loss of ~6.7% at ~520 °C, which is linked to the as-synthesized Co_3O_4. This is because the as-synthesized Co_3O_4 contains 6.7 wt% of amorphous carbon which is very likely to be burnt off at 520 °C. In order to avoid the collapse of the structure of the Co-CPs, the Co-CPs are calcined in a tube furnace at 500 °C under air.

Fig. 3 shows the XRD patterns of Co_3O_4 after the Co-CPs are calcined at 500 °C for 30 min. The sharp peaks indicate that the as-prepared Co_3O_4 samples are highly crystalline, and no impurity peaks are observed. All diffraction peaks of the XRD patterns of Co_3O_4-A, Co_3O_4-B and Co_3O_4-C can be

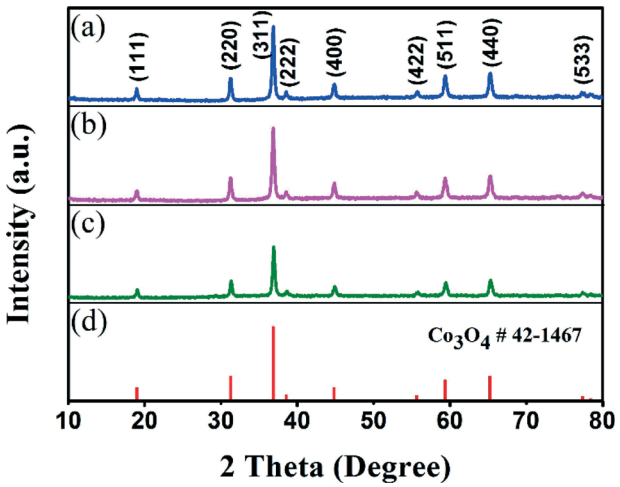

Fig. 3 XRD patterns of the as-prepared Co_3O_4 samples: (a) Co_3O_4-A, (b) Co_3O_4-B, (c) Co_3O_4-C and (d) the standard data of Co_3O_4 from JCPDS card no. 42-1467.

indexed as the *fcc* phase (JCPDS card no. 42-1467) with the space group *Fd3m* and lattice constant α = 8.08 Å. Based on the full width at half maximum (FWHM), the crystallite size of the as-synthesized samples can be estimated from the peak width using the Debye–Scherrer equation as follows:

$$D = 0.89\gamma/B\cos\theta$$

In this formula, B denotes the value of the FWHM. The diffraction peaks were fitted to a Gaussian function. The average particle sizes are calculated to be 33.1 nm, 41.4 nm and 53.5 nm for Co_3O_4-A, Co_3O_4-B and Co_3O_4-C, respectively.

The previous SEM images (Fig. 1a′–c′) and the TEM images (shown in Fig. 4) present the particle morphologies of the Co_3O_4 samples after pyrolysis based on the Co-CPs with various structures. The morphologies of the Co_3O_4 samples are composed of clustered porous nanoparticles with sizes of about 30 nm, in which the pore size between the particles appears to be less than 5 nm. As shown in the SEM (Fig. 1a′–c′) and TEM images (Fig. 4), the morphologies and pore sizes of Co_3O_4 depend on the structures of the precursors of Co-CPs. Co_3O_4-A presents pieces with a paper-like morphology, which are composed of single crystallites with relatively big pore sizes. Co_3O_4-B presents the opened-book like morphology of the pieces of nanosheets, and Co_3O_4-C presents the closed-book like morphology of the nanoparticles with the lowest pore size and distribution.

Nitrogen sorption isotherms are measured to gain information about the specific surface areas and pore sizes of the Co_3O_4 samples. As shown in Fig. 5a–c, the nitrogen adsorption–desorption isotherms with distinct hysteresis loops can be attributed to type IV curve, which suggest the presence of mesopores. Such mesopores are ascribed to the interparticle spaces caused by the random stacking of the Co_3O_4 nanoparticles. The values of the specific BET surface area (S_{BET}) of Co_3O_4-A, Co_3O_4-B, and Co_3O_4-C are determined to be 17.9, 17.4, and 12.2 $m^2\ g^{-1}$, respectively. Co_3O_4-A, with pieces of nanosheets, and Co_3O_4-B, with the opened book like morphology, present a slightly higher specific surface area than Co_3O_4-C, with the closed book like morphology. The evolution of the pore size distribution upon heat treatment is calculated based on the Barrett–Joyner–Halender (BJH) method. The pore size distribution plots (insets in Fig. 5a, b and c) reveal a bimodal distribution with a narrow distribution less than 5 nm. When the Co-CPs are converted to

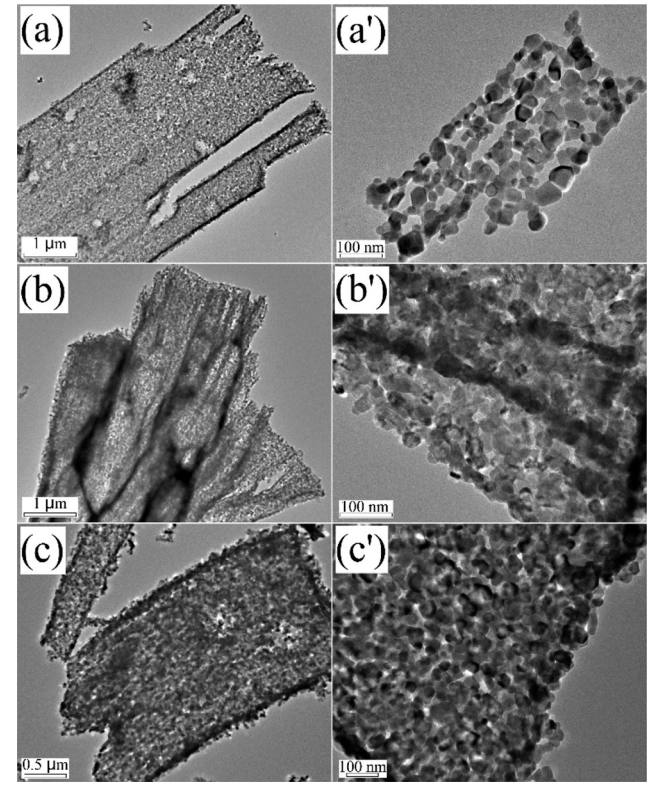

Fig. 4 TEM images of (a, a′) Co_3O_4-A, (b, b′) Co_3O_4-B and (c, c′) Co_3O_4-C.

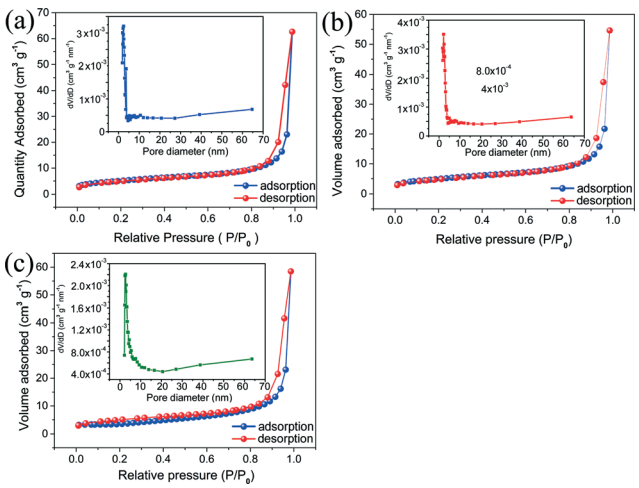

Fig. 5 N_2 adsorption–desorption isotherms and BJH pore size distribution plots (insets) of (a) Co_3O_4-A, (b) Co_3O_4-B and (c) Co_3O_4-C.

Co_3O_4, the carbon and nitrogen atoms of the ligands will be removed and lead to the formation of small pores.[24]

The porous structure of nanoparticles always provides appropriate Li ion diffusion lengths and a large contact area with electrolytes.[30] Poizot *et al.* suggest that for each metal oxide there is an optimum particle size and hence the best electrochemical performance.[31] They also revealed the electrochemical reaction occurring in the Co_3O_4 electrodes, as shown below:

$$Co_3O_4 + 8Li^+ + 8e^- \leftrightarrow 3Co + 4Li_2O$$

Cobalt metal and Li_2O form during the discharge process and then the nanosized metal particles decompose the Li_2O in the following step. Well-crystallized Co_3O_4 maintains the nanosized crystallite form and activates the decomposition of Li_2O. This is because the porous structure and high specific surface area of Co_3O_4-A and Co_3O_4-B are helpful for lithiation/delithiation.

3.2 Electrochemical measurement

Fig. 6 shows the first three cyclic voltammogram (CV) curves of the Co_3O_4 samples recorded at a scan rate of 0.1 mV s^{-1}. The initial CV curves of Co_3O_4-A, Co_3O_4-B and Co_3O_4-C present a pair of well-defined redox peaks at 1.96/1.03 V, 1.96/1.09 V and 1.96/0.86 V, respectively. The main difference between the initial CV profiles of the Co_3O_4 samples is the potential interval (ΔE) between the anodic peak and the corresponding cathodic peak. The ΔE is representative of the kinetic process, especially considering that the electrochemical process involves lithium diffusion in the solid phase and electron jumping across the electrodes.[32] Co_3O_4-B shows the smallest value of ΔE (0.87 V) compared to Co_3O_4-A (0.93 V) and Co_3O_4-C (1.10 V), respectively. The opened book-like morphology of Co_3O_4-B provides an efficient way for the lithiation/delithiation processes to occur, compared with the accumulated pieces with the paper-like morphology of Co_3O_4-A and the closed overlapped morphology of Co_3O_4-C. In the following two CV cycles, the redox peaks of Co_3O_4-A and Co_3O_4-C shift to a much higher voltage in the anodic process and to a much lower value in the cathodic process, and are associated with the peak current decreases (as shown in Fig. 6), while those of Co_3O_4-B almost remain at the same peak positions. The response and reversibility of Li^+ are weakened in Co_3O_4-A and Co_3O_4-C. The accumulation of pieces of the Co_3O_4-A nanosheets and the self-assembled closed book-like morphology of Co_3O_4-C hinder the lithium diffusion ability during the redox processes, which are reflected in their poor electrochemical responses. The well-defined peaks and smallest ΔE of Co_3O_4-B show the enhancement of the electrochemical reversibility and the lower ohmic resistance in the electrode reaction. It can be explained that the opened book-like morphology of Co_3O_4-B may provide an effective lithium diffusion channel for the redox lithiation/delithiation processes.

Fig. 7 shows the initial charge–discharge profiles and cycle performances of the Co_3O_4 samples at a current of 100 mA g^{-1}. In the initial discharge curve, it can be seen that there are two sloping potential ranges for the lithium reaction, which is similar to the previous reports.[17,33]

Two potential plateaus at ~1.26 and ~1.23 V (*vs.* Li/Li^+), corresponding to the reduction of Co^{3+}/Co^{2+} and Co^{2+}/Co, are shown in the discharge curves.[34] As shown in the left panel of Fig. 7, the initial discharge capacities of Co_3O_4-A, Co_3O_4-B and Co_3O_4-C are 1216, 1408 and 1151 mA h g^{-1}, respectively. All of these values are higher than the theoretical capacity (890 mA h g^{-1}). This phenomenon has been explained by irreversible reactions to form SEI films and possibly interfacial lithium storage.[30,35] After 50 cycles, the reversible capacities of Co_3O_4-A, Co_3O_4-B and Co_3O_4-C decrease to 536, 651 and 391 mA h g^{-1}, respectively. The coulomb efficiencies of Co_3O_4-A, Co_3O_4-B and Co_3O_4-C are close to 100%, except for the first several cycles. Furthermore, the cyclic performance of the Co_3O_4-B with an opened book-like morphology is substantially better than those of Co_3O_4-A (pieces of paper-like nanosheets) and Co_3O_4-C (closed book-like morphology). However, as shown in Fig. 7, the capacities of Co_3O_4-B during the first few cycles are higher than its theoretical capacity. Several previous reports revealed that the discharge capacity of Co_3O_4 was higher than its theoretical capacity, because extra Li^+ would be stored in the SEI films and pores of the

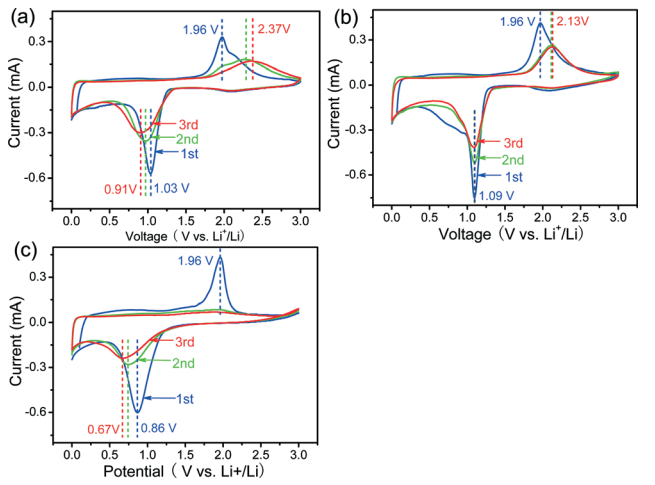

Fig. 6 The first three CV curves of (a) Co_3O_4-A, (b) Co_3O_4-B and (c) Co_3O_4-C at a scan rate 0.1 mV s^{-1}.

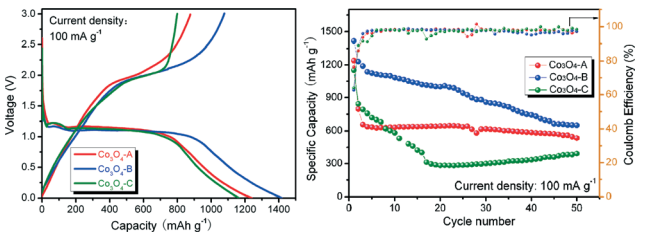

Fig. 7 (left) The first charge–discharge cycles of the Co_3O_4 electrodes tested at a rate of 100 mA g^{-1}, (right) the cycle performance of the Co_3O_4 at a current density of 100 mA g^{-1}.

porous anode material.[18,24,29,30,35,36] In this work, Co-CP-B as a template provides the frame of the opened book-like structure during the pyrolysis at 500 °C. The porous structure of Co_3O_4-B provides tunnels and results in a large number of Li^+ ions involved in the lithiation and following delithiation. By comparison, the accumulated nanosheets of Co_3O_4-A and closed overlapped Co_3O_4-C nanoparticles hinder more lithium cations and prevent their involvement in the lithiation/delithiation processes of Co_3O_4, thus presenting relatively low capacities. The morphology of Co_3O_4 plays an important role in the high performance anode materials for lithium batteries. However, Co_3O_4-B delivers 1408 mA h g^{-1} but only remains at 651 mA h g^{-1} after 50 cycles, although the final value is higher than the values of 536 and 391 mA h g^{-1} for Co_3O_4-A and Co_3O_4-C, respectively. The capacity fading of Co_3O_4-B is worse than that of Co_3O_4-A and Co_3O_4-C. It might be due to the fact that the opened book-like morphology has good lithiation/delithiation ability in the first few cycles and delivers a high specific capacity, but the channel for lithium diffusion in Co_3O_4-B may be jammed by the formation of SEI films and the aggregation of the nanoparticles during the following charge–discharge cycles. After dozens of charge–discharge cycles, Co_3O_4-B presents a somewhat higher specific capacity than Co_3O_4-A and Co_3O_4-C.

Further evidence of the high power performance of the Co_3O_4 samples is obtained through the rate capacity performance measurements. The galvanostatic charge–discharge curves and cyclic rate performances of Co_3O_4-A, Co_3O_4-B and Co_3O_4-C at different current rates are presented in Fig. 8. The plateau voltages shift toward higher potentials in charging curves and decrease to lower potentials in discharging curves with an increase in the current rate, and thus the Co_3O_4 samples show gradually reduced storage capacities. Co_3O_4-B with an opened book-like morphology delivers a good rate capability, with discharge capacities of 1552, 919, 751, 663 and 574 mA h g^{-1} at current densities of 40, 100, 400, 800 and 1200 mA g^{-1}, respectively. By comparison, Co_3O_4-A and Co_3O_4-C show poor rate performances of 556 and 432 mA h g^{-1} (Co_3O_4-A), and 126 and 56 mA h g^{-1} (Co_3O_4-C) at 800 and 1200 mA g^{-1}, respectively, because the fast extraction and reinsertion of lithium cations are hindered by the accumulated structures of the Co_3O_4 nanoparticles. Co_3O_4-C presents a strange initial charge curve at 40 mA g^{-1} in Fig. 8c. This strange charge curve only appears at a current density of 40 mA $g^{-1}$and disappears beyond 100 mA g^{-1} (ESI† Fig. S3). The re-measured results still show the strange curve and the reason is still unknown.

Fig. 9 presents the cyclic performance of the Co_3O_4 samples at a current density of 800 mA g^{-1}. Co_3O_4-A, Co_3O_4-B and Co_3O_4-C release initial capacities of 1090, 1181 and 843 mA h g^{-1}, respectively. The capacities of Co_3O_4-A and Co_3O_4-C are 497 and 131 mA h g^{-1} after 50 cycles, but that of Co_3O_4-B remains at 597 mA h g^{-1} after 50 cycles. The coulomb efficiencies of the three samples are close to 100% except for the first several charge–discharge cycles, because significant irreversible capacities are consumed on the formation of SEI films and the delithiation process is decreased.[30,35]

Electrochemical impedance spectroscopy (EIS) is carried out to identify the charge transfer resistance in the electrode materials with various morphologies. The Nyquist plots (imaginary part, Z_{im}, *versus* real part, Z_{re}) of the Co_3O_4-A, Co_3O_4-B and Co_3O_4-C electrodes in the frequency range from 100 kHz to 10 mHz are shown in Fig. 10. The EIS curves exhibit a semicircular pattern in the high frequency range and a straight line in the low frequency region. The semicircular patterns have a high-frequency intercept at the Z' axis that represents the resistance of the lithium ion migration

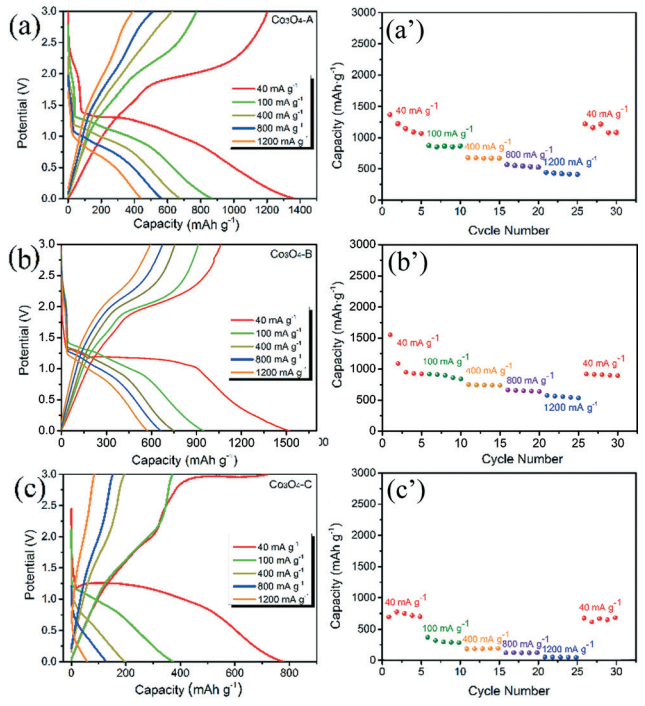

Fig. 8 Voltage profiles of the porous sheet-based Co_3O_4 at different current densities in a coin-type lithium cell, and the rate performance with increasing charge–discharge current densities from 40 to 1200 mA g^{-1}. (a, a') Co_3O_4-A, (b, b') Co_3O_4-B and (c, c') Co_3O_4-C.

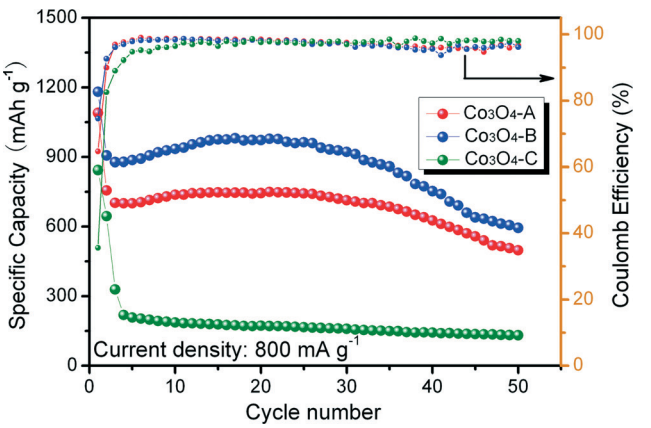

Fig. 9 The cyclic performances of Co_3O_4-A, Co_3O_4-B and Co_3O_4-C at a current density of 800 mA g^{-1}.

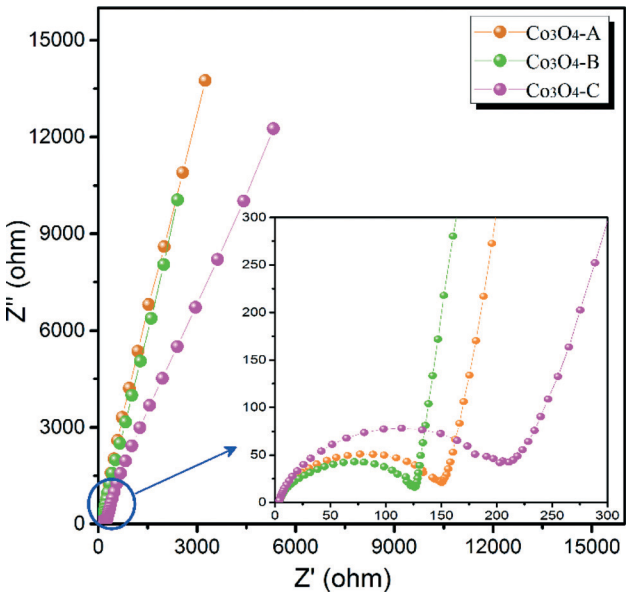

Fig. 10 Nyquist plots of the Co_3O_4-A, Co_3O_4-B and Co_3O_4-C anode materials.

through the interface between the surface layer of the particles and the electrolyte. The low-frequency tail is attributed to the diffusion process of the lithium ions in the bulk of the electrode material and the Warburg resistance. As shown in Fig. 10, Co_3O_4-B presents lower high-frequency resistance than Co_3O_4-A and Co_3O_4-C, about 150, 126 and 217 ohms in Co_3O_4-A, Co_3O_4-B and Co_3O_4-C, respectively. The electrode composed of the Co_3O_4-B displays significant electrochemical performance. It has been suggested that the opened book-like morphology of Co_3O_4-B provides efficient lithium diffusion tunnels and increases the electrolyte/Co_3O_4 contact area.

Fig. 11 shows the EIS plots of the Co_3O_4 electrodes at the 6th full discharge and the 7th full charge states. At the full discharge state, Co_3O_4 converts to Co metal after lithiation, and the Co metal reacts with Li_2O during the delithiation at the full charge state. The resistance of the electrodes at the full discharge state (as shown by the blue date points in Fig. 11) is much lower than the value at the full charge state (as shown by the red data points in Fig. 11). The Co_3O_4-A, Co_3O_4-B and Co_3O_4-C samples present similar resistances at the full discharge state because of the excellent conductivity of the Co metal. But Co_3O_4-B presents a relatively smaller resistance than Co_3O_4-A and Co_3O_4-C, which might be due to the fact that the opened book-like morphology of Co_3O_4 is stable and provides an efficient way to maintain conductivity during the charge–discharge cycles.

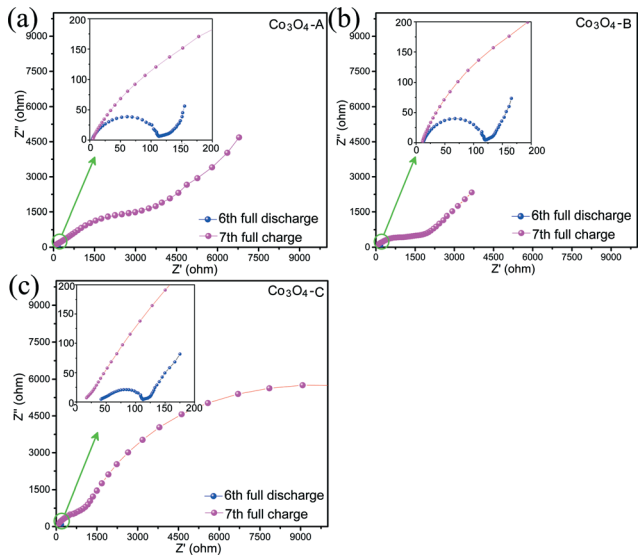

Fig. 11 EIS plots of the Co_3O_4 electrodes at the 6th full discharge and the 7th full charge states.

4 Conclusions

In summary, a series of Co coordination frameworks are synthesized under various solvothermal conditions. The two-dimensional frameworks, agglomerated by Co_3O_4 nanoparticles, remained after the pyrolysis of the Co-CPs. The morphology of Co_3O_4 plays an important role in the high performance anode materials for lithium batteries. The accumulated nanosheets of Co_3O_4 and closed overlapped Co_3O_4 nanoparticles hinder the lithium cations and prevent their involvement in the lithiation/delithiation processes of Co_3O_4, and present relatively low capacities. Co_3O_4 nanoparticles with an opened book-like morphology deliver a high capacity of 597 mA h g^{-1} after 50 cycles at 800 mA g^{-1}. Co_3O_4 with an opened book-like morphology provides efficient lithium diffusion tunnels, increases the electrolyte/Co_3O_4 contact area and delivers an outstanding rate capacity of 574 mA h g^{-1} at a current density of 1200 mA g^{-1}.

Acknowledgements

This research was supported by the National Natural Science Foundation (51072072, 51272095, 51172032). The authors also acknowledge financial support from the European Union Marie Curie FP7-IRSES project (no: 295208).

Notes and references

1 R. Fong, R. U. von Sacken and J. R. Dahn, *J. Electrochem. Soc.*, 1990, **137**, 2009.
2 W. J. Zhang, *J. Power Sources*, 2011, **13**, 196.
3 J. Y. Huang, L. Zhong, C. M. Wang, J. P. Sullivan, W. Xu, L. Q. Zhang, S. X. Mao, N. S. Hudak, X. H. Liu, A. Subramanian, H. Fan, L. Qi, A. Kushima and J. Li, *Science*, 2010, **330**, 1515.
4 P. Poizot, S. Laruelle, S. Grugeon, L. Dupont and J.-M. Tarascon, *Nature*, 2000, **407**, 496.
5 K. T. Nam, D. P. Kim, J. Yoo, C. Chiang, N. Meethong, P. T. Hammond, Y. Chiang and A. M. Belcher, *Science*, 2006, **312**, 885.
6 C. Ban, Z. Wu, D. T. Gillaspie, L. Chen, Y. Yan, J. L. Blackburn and A. C. Dillon, *Adv. Mater.*, 2010, **22**, E145.

7 H. Y. Wang, P. Gao, S. F. Lu, H. D. Liu, G. Yang, J. Pinto and X. F. Jiang, *Electrochim. Acta*, 2011, **58**, 44.
8 G. S. Wang, Y. Deng and L. Guo, *Chem. – Eur. J.*, 2010, **16**, 10220.
9 L. N. Jin, Q. Liu and W. Y. Sun, *CrystEngComm*, 2012, **14**, 7721.
10 Y. Chen, Y. Zhang and S. Fu, *Mater. Lett.*, 2007, **61**, 701.
11 A. Rumplecker, F. Kleitz, E.-L. Salabas and F. Schueth, *Chem. Mater.*, 2007, **19**, 485.
12 K. V. Rao and C. S. Sunandana, *Solid State Commun.*, 2008, **148**, 32.
13 X. W. Lou, D. Deng, J. Y. Lee and L. A. Archer, *J. Mater. Chem.*, 2008, **18**, 4397.
14 C. Xu, J. Sun and L. Gao, *CrystEngComm*, 2011, **13**, 1586.
15 C. C. Li, X. M. Yin, T. H. Wang and H. C. Zeng, *Chem. Mater.*, 2009, **21**, 4984.
16 D. Wang, Q. Wang and T. Wang, *Inorg. Chem.*, 2011, **50**, 6482.
17 F. M. Zhan, B. Y. Geng and Y. J. Guo, *Chem. – Eur. J.*, 2009, **15**, 6169.
18 X. Wang, H. Guan, S. Chen, H. Q. Li, T. Y. Zhai, D. M. Tang, Y. Bando and D. Golberg, *Chem. Commun.*, 2011, **47**, 12280.
19 L. Hu, Q. Peng and Y. Li, *J. Am. Chem. Soc.*, 2008, **130**, 16136.
20 S. Jung, W. Cho, H. J. Lee and M. Oh, *Angew. Chem., Int. Ed.*, 2009, **48**, 1459.
21 W. Cho, Y. H. Lee, H. J. Lee and M. Oh, *Chem. Commun.*, 2009, 4756.
22 W. Cho, S. Park and M. Oh, *Chem. Commun.*, 2011, **47**, 4138.
23 Y. Lu, H. Cao, S. Zhang and X. Zhang, *J. Mater. Chem.*, 2011, **21**, 8633.
24 L. Hu, N. Yan, Q. W. Chen, P. Zhang, H. Zhong, X. R. Zheng, Y. Li and X. Y. Hu, *Chem. – Eur. J.*, 2012, **18**, 8971.
25 F. Meng, Z. G. Fang, Z. X. Li, W. W. Xu, M. J. Wang, Y. P. Liu, J. Zhang, W. R. Wang, D. Y. Zhao and X. H. Guo, *J. Mater. Chem. A*, 2013, **1**, 7235.
26 B. Liu, X. B. Zhang, H. Shioyama, T. Mukai, T. Sakai and Q. Xu, *J. Power Sources*, 2010, **195**, 857.
27 W. D. Shi, S. Y. Song and H. J. Zhang, *Chem. Soc. Rev.*, 2013, **42**, 5714.
28 A. Banerjee, P. Mahata and S. Natarajan, *Eur. J. Inorg. Chem.*, 2008, 3501.
29 O. M. Yaghi, H. L. Li and T. L. Groy, *J. Am. Chem. Soc.*, 1996, **118**, 9096.
30 N. Yan, L. Hu, Y. Li, Y. Wang, H. Zhong, X. Y. Hu, X. K. Kong and Q. W. Chen, *J. Phys. Chem. C*, 2012, **116**, 7227.
31 P. Poizot, S. Laruelle, S. Grugeon, L. Dupont and J. M. Tarascon, *Nature*, 2000, **407**, 496.
32 F. Croce, A. D. Epifanio, J. Hassoun, A. Deptula, T. Olczac and B. Scrosati, *Electrochem. Solid-State Lett.*, 2002, **5**, A47.
33 D. Fang, L. C. Li, W. L. Xu, G. Z. Li, G. Li, N. F. Wang, Z. P. Luo, J. Xu, L. Liu, C. L. Huang, C. W. Liang and Y. S. Ji, *J. Mater. Chem. A*, 2013, **1**, 13203.
34 B. G. Choi, S. J. Chang, Y. B. Lee, J. S. Bae, H. J. Kim and Y. S. Huh, *Nanoscale*, 2012, **4**, 5924.
35 W. Y. Li, L. N. Xu and J. Chen, *Adv. Funct. Mater.*, 2005, **15**, 851.
36 J. Y. Wang, N. L. Yang, H. J. Tang, Z. H. Dong, Q. Jin, M. Yang, D. Kisailus, H. J. Zhao, Z. Y. Tang and D. Wang, *Angew. Chem.*, 2013, **125**, 6545.

